An Elastoplastic Finite Element Study of Displacement-Controlled Fretting in a Plane-Strain Cylindrical Contact

Huaidong Yang
Georgia Institute of Technology,
G. W. Woodruff School of
Mechanical Engineering,
Atlanta, GA 30332-0405
e-mail: hyang380@gatech.edu

Itzhak Green
Georgia Institute of Technology,
G. W. Woodruff School of
Mechanical Engineering,
Atlanta, GA 30332-0405
e-mail: green@gatech.edu

This work presents a finite element study of a two-dimensional (2D) plane strain fretting model of a half cylinder in contact with a flat block under oscillatory tangential loading. The two bodies are deformable and are set to the same material properties (specifically steel), however, because the results are normalized, they can characterize a range of contact scales (micro to macro), and are applicable for ductile material pairs that behave in an elastic-perfectly plastic manner. Different coefficients of friction (COFs) are used in the interface. This work finds that the edges of the contacting areas experience large von Mises stresses along with significant residual plastic strains, while pileup could also appear there when the COFs are sufficiently large. In addition, junction growth is investigated, showing a magnitude that increases with the COF, while the rate of growth stabilization decreases with the COF. The fretting loop (caused by the tangential force during the fretting motion) for the initial few cycles of loading is generated, and it compares well with reported experimental results. The effects of boundary conditions are also discussed where a prestressed compressed block is found to improve (i.e., reduce) the magnitude of the plastic strain compared to an unstressed block. [DOI: 10.1115/1.4038984]

1 Introduction

Fretting occurs when two contacting surfaces experience small amplitude of oscillatory relative motion under normal load. Depending on whether a stick area exists or not, steady-state fretting regimes can be divided into partial slip and gross slip. Partial slip conditions are mainly responsible for the mechanical failure of surface crack initiation and propagation, while gross slip conditions introduce wear [1]. The objective here is to form an in-depth understanding of the mechanisms of fretting wear, and the propensity for crack initiation and propagation.

The theoretical analysis of fretting is addressed by Johnson [2]. He provides elastic solutions of contact pressure, tangential force, and deformation on the contacting surface, addressing both cylindrical and spherical contacts in situations of partial and gross slip. Additionally, Cattaneo [3] and Mindlin [4] address the stress distribution of the surface and subsurface for spherical partial slip. The complete stress field of spherical sliding contacts is further developed by Goodman and Hamilton [5]. The cylindrical plane-strain contact is investigated by Adams [6], considering stick, partial slip, and sliding.

The fretting phenomenon has been thoroughly investigated experimentally. The first experimental work can be traced back to Courtney-Pratt and Eisner [7]. They study a sphere-over-flat contact between metallic materials under oscillatory tangential force. They focus on the initial stage of oscillatory tangential load but do not include the wear and fatigue caused by thousands of load cycles. The horizontal displacement of the upper ball and the tangential force are recorded and the contact area is found indirectly by measuring the electrical conductance. Junction growth, i.e., the increase in the contact area, and also the hysteresis loops of tangential force are reported. The junction growth under the fretting load condition is also reported by Tabor [8] and by Parker and Hatch [9]. Tabor considers the effect of contamination, which can reduce the strength of the material, and shows that the limit of growth is decreased when the interface is five percent weaker than the bulk material. Parker and Hatch [9] measure the contact area via an optical method between soft spheres (lead or indium) and a glass flat.

Following the study with initial fretting cycles, fretting wear and fatigue are studied experimentally [10–12]. They study crossed-cylinders and ball-on-flat contacts but not the cylindrical line contact. The fretting studied by Leonard et al. [10] occurs on the coating material of Tungsten carbide reinforced amorphous hydrocarbon (WC/a-C: H) and chromium nitride (Cr2N). Both coatings are found to be effective to reduce wear. Warhadpande et al. [12] study the effect of fretting wear on the contact fatigue life of M50 bearing steel. The results show that under a normal load, an elastic-plastic fretting scar can reduce the fatigue life by 30 percent. Apart from the unlubricated conditions, Leonard et al. [13] investigate the lubricated fretting contacts. Gaseous cavitation is observed on the trailing edge of the contact, which is very likely to close the passage for the lubricant to reach the contact area.

Although ample experimental work has been done on fretting, the theoretical analysis lacks any modeling of fretting at the regimes of elastic-plastic and fully plastic contacts, especially for cylindrical contacts. The elastic-plastic and fully plastic spherical contacts in strictly normal loading have been studied in great details, using the finite element analysis (FEA) method [14–16].

Contributed by the Tribology Division of ASME for publication in the Journal of Tribology. Manuscript received October 17, 2017; final manuscript received December 30, 2017; published online February 22, 2018. Assoc. Editor: Sinan Muftu.

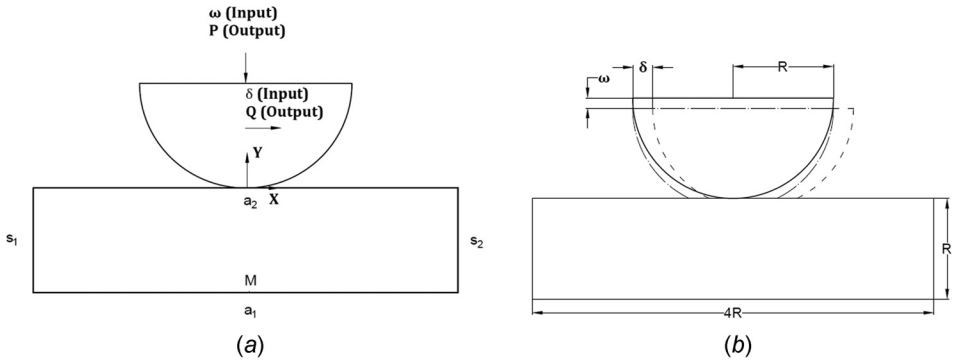

Fig. 1 Schematic of a half-cylinder in contact with a flat block, along with the loading definitions: (*a*) displacement-controlled inputs and reaction outputs and (*b*) cylinder-block dimensions and displacement directions

The elastic-plastic cylindrical contact in plane stress is recently examined by Sharma and Jackson [17]. However, when tangential force is introduced under normal load, few attempts to analyze the contact have been made. Brizmer et al. [18] use the finite element method to investigate the spherical contact under the fully stick condition with tangential load. Junction growth is reported in all regimes of contact, elastic, elastic-plastic, and plastic. Chang and Zhang [19] model their contact without fully stick conditions and apply static frictional coefficient. Similar results of junction growth are found in the elastic-plastic regime. However, cylindrical contact, which is the prototype of contacts in gears, rolling element bearings, wheel on rail, and human joints, is not considered in the above work.

The work by Vijaywargiya and Green [20] presents the results of a finite element analysis used to simulate two-dimensional (2D) sliding between two interfering elastic-plastic cylinders. The material for the cylinders is modeled as elastic-perfectly plastic and follows the von Mises yield criterion. The FEA provides trends in the deformations, reaction forces, stresses, and net energy losses as a function of the interference and sliding distance between the cylinders. Results are presented for both frictionless and frictional sliding, and comparisons are drawn. The effects of plasticity and friction on energy loss during sliding are also given. The work by Boucly et al. [21] presents a semi-analytical method for the tridimensional elastic-plastic sliding contact between two hemispherical asperities using either a load-driven or a displacement-driven algorithm. They found the contact pressure distribution, the hydrostatic pressure, and the equivalent plastic strain state below the contacting surfaces. Pile-up induced by the permanent deformation of the bodies due to their relative motion is evident. A similar pile-up phenomenon is also present in the work reported here. However, while Refs. [20] and [21] do analyze the elastic-plastic damage done in the tugging of interfering bodies one across the other, sliding is applied in one direction only; that is, the repetitive (back-and-forth) fretting motion is not analyzed. The only work of parallel cylindrical fretting contact found so far is [22,23]. Gupta et al. [22] develop a model that consists of a meager 285 elements and is limited by the computational memory typically available in 1993. Ghosh et al. [23] simulate the fretting wear of Hertzian line contact in partial slip. The von Mises stress profiles and tangential force loops of fretting are found in that work. But the results are not presented in a nondimensional form. Also, the effects of the coefficients of friction (COF), normal load, and plastic deformation are not considered. With current computing capabilities, the accuracy of these results can be improved considerably and that is one of the aims of this work. First, modeling is performed with sufficiently fine and adaptive meshes that capture the behavior in the contact region with great accuracy. Then, the results are reported in a nondimensional form to allow their broader utility. Finally, this work examines the effects of boundary conditions upon the results, underlining potential strategies to lessen the damaging effects of fretting.

Fretting can happen under specified loads, specified displacements, or a combination of both. The outcomes of displacement- and load-controlled fretting are different in wear tests according to Mohrbacher et al. [24]. Displacement-controlled fretting is applicable to conditions when the contacting elements are confined within prescribed spaces, such as prosthetic knee joints [25–27], bolted joints and interference (press) fits [28,29], as well as cutting tools in machining [30]. Therefore, the understanding of displacement-controlled fretting is useful for these and similar applications, and it is, hence, the impetus of this work.

In this work, the finite element approach, using ANSYS 17.1, is applied to analyze the fretting damage for a 2D plane-strain contact between a half cylinder and a flat block of identical isotropic and homogeneous steels. The model is a half-cylinder in contact with a flat block. As shown in Fig. 1, the loading inputs are a vertical interference, ω, and the following oscillatory horizontal displacement, δ, forced upon the cylinder while the block is held fixed. The said normal interference and horizontal displacement generates corresponding reactions P and Q, respectively, which are outputs obtained from the FEA results. The normal loading is done in regimes ranging from purely elastic to elastic-plastic contacts. Five aspects of the fretting model are investigated: the development of the von Mises stresses and plastic strains near the contacting surfaces, the junction growths, the evolution of the tangential forces in the initial few cycles of oscillatory tangential loads, and the scars on the surface of the block. The effects of the COFs, normal interferences, and the boundary conditions on the block are also investigated. The results of this work are found to agree well with former related experimental data.

2 The Model

Figure 1(*a*) presents a half cylinder of a radius $R = 0.5$ m in contact with a $4R \times R$ block. In the figure, the axes of X and Y are shown where the origin is located at the contact point. The four sides of the block are represented by letters a_1, a_2, s_1, and s_2. The cylinder and the block are set to the same material properties, i.e., elastic modulus $E = 200$ GPa, Poisson's ratio $\nu = 0.32$, and yield strength $S_y = 0.9115$ GPa. The material is modeled to behave as elastic-perfectly plastic. Adhesion is not considered in this work.

The fretting model is now introduced. As shown in Fig. 1(*b*), the cylinder radius is R; block dimensions are given in terms of that radius, and this is maintained throughout this work. First, a vertical displacement, ω, on the top of the half cylinder is applied. That is referred to as the interference. While keeping the interference constant, horizontal oscillations, δ, are then applied to simulate the fretting motion. That is, the top of the half cylinder is

forced to displace a certain distance to the right first, and then forced back to the left passing the origin position, continuing the same distance to the left, before returning back to the origin—that constitutes one cycle of loading. The procedure is performed quasi-statically, taking 40 load steps to complete one cycle. It is henceforth implicitly understood that "right" or "left" ascribe motion direction or location in the positive or negative X axis, respectively.

In an elastic contact regime, the solution of the 2D plane-strain cylindrical contact is given by the Hertzian contact model [2]. Under a total load per unit length, P/L, the maximum pressure, p_0, is located at the center of the contact

$$p_0 = \frac{2P}{\pi bL} \tag{1}$$

where the half-width of contact, b, is given as

$$b = \left(\frac{4PR}{\pi LE'}\right)^{\frac{1}{2}} \tag{2}$$

where E' is the equivalent elastic modulus given by [31]

$$\frac{1}{E'} = \frac{1-\nu_1^2}{E_1} + \frac{1-\nu_2^2}{E_2} \tag{3}$$

The interference of a half cylinder in contact with a block, whose depth is R, is given in the Appendix

$$\omega = \frac{P/L}{2\pi E'}\left\{2\ln\left(\frac{2\pi RE'}{P/L}\right) - \frac{1}{1-\nu}\right\} \tag{4}$$

The critical half contact width, b_c, and the load per unit length, P_c/L, at which the maximum von Mises stress reaches the yield strength, S_y, are derived by Green [32], where $C(\nu) = 1.164 + 2.975\nu - 2.906\nu^2$, for $\nu > 0.1938$. These are

$$b_c = \frac{2RCS_y}{E'} \tag{5}$$

$$\frac{P_c}{L} = \frac{\pi R(CS_y)^2}{E'} \tag{6}$$

By substituting Eq. (6) into Eq. (4), the critical interference is

$$\omega_c = \frac{R}{2}\left(\frac{CS_y}{E'}\right)^2\left[4\ln\left(\frac{\sqrt{2}E'}{CS_y}\right) - \frac{1}{1-\upsilon}\right] \tag{7}$$

For the material properties herein, $C = 1.818$, $\omega_c = 0.000927$ m, $b_c = 0.0149$ m, and $P_c/L = 3.873 \times 10^7$ N/m. These values are used to normalize the forthcoming results.

In this work, the values of the vertical interference are integer multiples of the critical one, namely, $1^*\omega_c$, $2^*\omega_c$, $3^*\omega_c$, etc. The amplitude of the horizontal displacement is always kept equal to the critical interference, $1^*\omega_c$. In this way, the results are readily nondimensionalized and they can be applied to both macroscopic and microscopic contacts. With the inputs of ω and δ, the normal and tangential forces at the contact, P and Q, are obtained, respectively, from the simulation. Hence, this is a displacement controlled simulation.

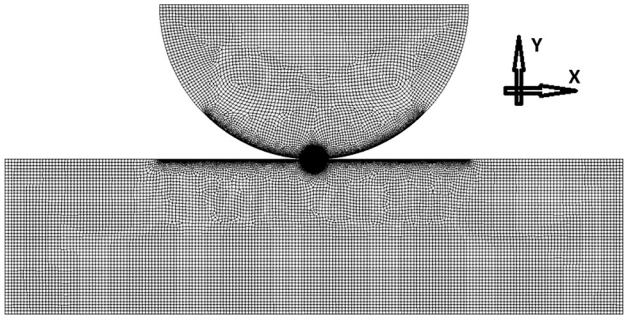

Fig. 2 Finite element model in ANSYS 17.1

3 The Mesh

A 2D plane-strain element (PLANE183) is used in ANSYS 17.1 to model the contact (see Fig. 2). The total mesh consists of 59,806 elements, where the mesh in the contact area is refined with the element length size of 0.0004 m. One hundred contact elements are defined on each side of the contact. Stiff springs are attached to these elements and activated once penetration is incipient. This is intrinsically handled by ANSYS contact and target elements named CONTA172 and TARGE169.

To validate the model, mesh convergence is first performed for the elastic contact (interference ranges from $0.2^*\omega_c$ to $1^*\omega_c$) and the results are compared with those from Hertz contact solution. For the comparison, ω/ω_c is the input, ω_c is calculated by Eq. (7), and thus ω is imposed in the FEA. The theoretical load per length, P/L, is solved from Eq. (4), while in the FEA simulation P/L is the reaction output. From the entire interference range examined in Table 1, for $d/R = 1$, the load per unit length differs by a maximum of 0.47%, the contact width by 2.17%, the maximum contact pressure by 1.57%, and the maximum von Mises stress by 1.09% (The prediction $\sigma_{emax} = p_0/C$ is according to Green [32]. Herein, $R = 0.5$ m, $\nu_1 = \nu_2 = 0.32$, and $E_1 = E_2 = 200$ GPa). Additional comparisons are also given in the Appendix for different block sizes at the critical interference. With such outstanding agreement between theoretical and FEA results, the model and mesh convergence have been established.

In addition, there is no closed-form solution for elastic-plastic contacts under the combined load of normal and tangential loads. For such cases, the elements of the mesh are iteratively refined by a factor of two until there is less than one percent difference in the contact width between iterations. Additionally, the region in contact is always confined within the refined mesh.

4 Results and Discussion

The following results are reported for specific boundary conditions applied on the block (shown in Fig. 1(*a*)): The base of the

Table 1 Comparison of selected values between theoretical predictions and FEA results for a half-cylinder of radius, *R*, in elastic contact with a $4R \times R$ block (ω ranges from $0.2^*\omega_c$ to $1^*\omega_c$)

	Theoretical predictions					FEA results							
Input ω/ω_c	Eq. (7) ω (mm)	Eq. (2) b (mm)	Eq. (4) P/L (MN/m)	Eq. (1) p_0 (GPa)	p_0/C σ_{emax} (GPa)	b (mm)	% dif	P/L (MN/m)	% dif	p_0 (GPa)	% dif	σ_{emax} (GPa)	% dif
0.2	0.1854	6.03	6.36	0.672	0.3693	6.04	−0.41	6.33	−0.43	0.661	−1.57	0.3675	−0.50
0.6	0.5562	11.15	21.75	1.242	0.6830	11.20	0.48	21.65	−0.47	1.231	−0.86	0.6904	1.09
1	0.9266	14.88	38.73	1.657	0.9115	15.20	2.17	38.56	−0.43	1.645	−0.75	0.9122	0.08

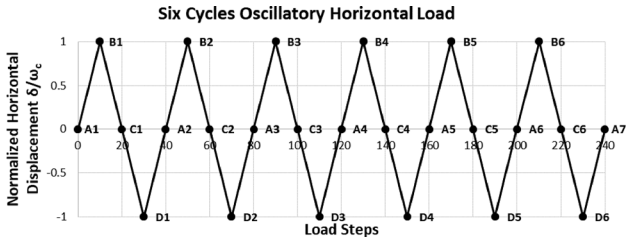

Fig. 3 Load stepping of six cycles oscillatory horizontal load

block, a_1, is fixed in both the X and Y directions, and the other three sides of the block (a_2, s_1, and s_2) are free. The effects of other boundary conditions will be discussed at the end of the paper. The results of the finite element model are presented using the normalized vertical interference, $\omega^* = \omega/\omega_c$, ranging from 0.7 (initially inducing a purely elastic regime) to three (initially inducing an elastic-plastic regime [15], where the plasticity reaches the surface). Four different frictional coefficients are imposed at the contact interface, 0.1, 0.3, 0.45, and 1. In order to describe the oscillatory horizontal displacement, load steps are used. As shown in Fig. 3, Step 0 represents the start of horizontal load just after the vertical interference is applied. Each step increment represents a sliding distance of $0.1*\omega_c$. It takes 40 steps to complete one cycle of loading. Due to the computational burden (20 h for a single simulation on a 3 GHz Intel Xeon personal computer Workstation), the maximum number of horizontal displacement cycles investigated in this work is set to six.

The following convention of notation is used to signify the location and the cycle number. Points (A,B,C,D) signify, respectively, $\delta = (0,1,0,-1)\omega_c$, and $n = 1,2,\ldots,6$ specifies the cycle number. For example, A4 represents the inception of the fourth cycle, where $\delta = 0*\omega_c$.

4.1 The Evolution of von Mises Stress. Figure 4 shows the progression of von Mises stress at $1*\omega_c$ interference with $\mu = 1$ applied at the contact interface. The color-coding in each picture is maintained at the same scale. The darkest intensity color in the contact area indicates the maximum von Mises. The next two parameters are used to identify the horizontal load step. The first parameter represents the horizontal displacement, and the second

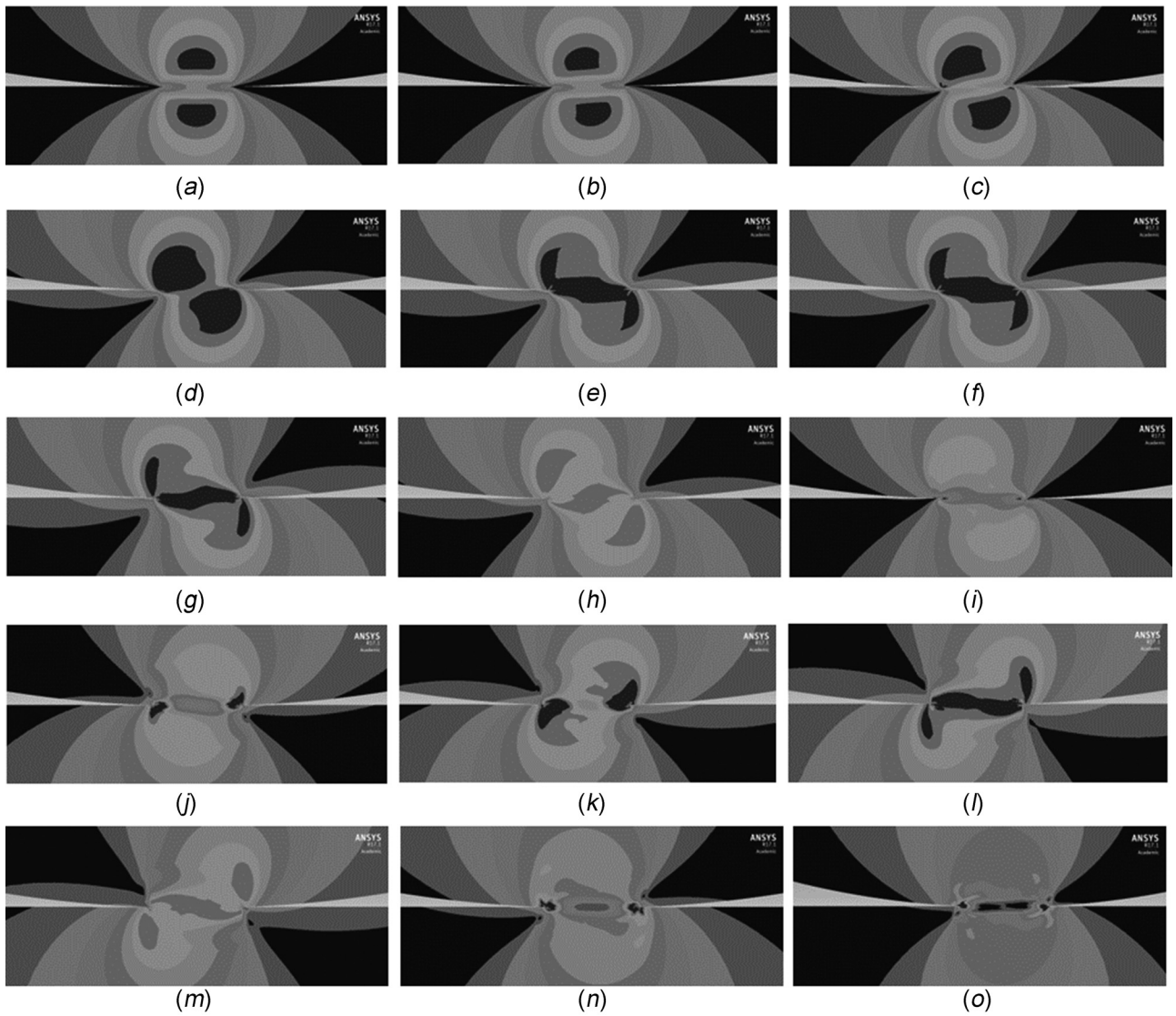

Fig. 4 Progression of von Mises stresses at $1*\omega_c$ vertical interference during the first cycle (*a*)–(*n*) and the last point (*o*) at the end of six cycles of horizontal loading with $\mu = 1$: (*a*) $0*\omega_c$ at A1-B1, (*b*) $0.1*\omega_c$ at A1-B1, (*c*) $0.3*\omega_c$ at A1-B1, (*d*) $0.5*\omega_c$ at A1-B1, (*e*) $0.6*\omega_c$ at A1-B1, (*f*) $0.7*\omega_c$ at A1-B1, (*g*) $1*\omega_c$ at A1-B1, (*h*) $0.9*\omega_c$ at B1-C1, (*i*) $0.5*\omega_c$ at B1-C1, (*j*) $0*\omega_c$ at B1-C1, (*k*) $-0.2*\omega_c$ at C1-D1, (*l*) $-1*\omega_c$ at C1-D1, (*m*) $-0.9*\omega_c$ at D1-A2, (*n*) $0*\omega_c$ at D1-A2, and (*o*) $0*\omega_c$ at D6-A7

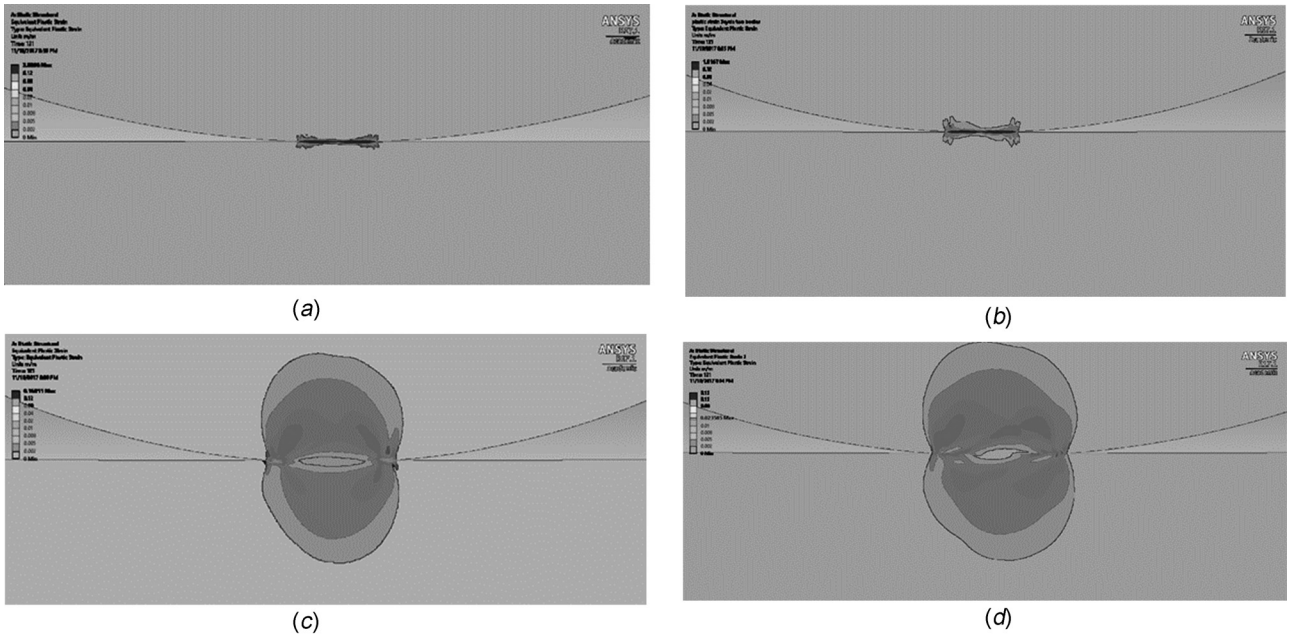

Fig. 5 The distribution of the equivalent plastic strain after three cycles of horizontal load near the contacting area: (*a*) 0.7*ω_c interference, $\mu = 1$, maximum $\varepsilon_p = 2.84$; (*b*) 1*ω_c interference, $\mu = 1$, maximum $\varepsilon_p = 1.82$; (*c*) 3*ω_c interference, $\mu = 1$, maximum $\varepsilon_p = 0.17$; and (*d*) 3*ω_c interference, $\mu = 0.3$, maximum $\varepsilon_p = 0.0024$

parameter indicates at which branch of the cycle the displacement is approached. For example, Figs. 4(*a*)–4(*g*) represent the horizontal displacement of the cylinder, $\delta = (0, 0.1, 0.3, 0.5, 0.6, 0.7, 1)*\omega_c$, respectively, in branch A1–B1 (defined in Fig. 3). Since the von Mises stress distributions in the cylinder and the block appear as mirror images, only the progressions of the von Mises stresses on the cylinder are discussed in the following.

At the very beginning, before horizontal displacement commences, the distribution of the von Mises stress (shown in Fig. 4(*a*)) solely represents a normal contact. The area with large von Mises stresses is located under the surface for $\nu > 0.1938$, in agreement with Green [32]. In this case, in Fig. 4(*a*), there is one point in each body reaching the yield strength. Then, the cylinder is forced to slide to the right (i.e., in the positive X direction). Depending on the value of the COF, the status of the contact region is gross sliding when $\mu = 0.1$ and 0.3, partial stick and partial slip when $\mu = 0.45$, or fully stick when $\mu = 1$, as indicated by ANSYS. The region of large von Mises stresses under the contacting surface is skewed to the left (Fig. 4(*b*)) due to the introduction of a tangential force acting in the direction opposite to the relative horizontal displacement. Then, another two regions of large von Mises stresses appear at the two edges of the contact (Fig. 4(*c*)). Afterward, the left plastic region merges with the one under surface (Fig. 4(*d*)) and then the two combined merge with the right one (Fig. 4(*e*)). As the cylinder moves further to the right, the region is stretched in the *x*-direction (Fig. 4(*f*)) until it reaches the amplitude of the displacement, $1*\omega_c$, (Fig. 4(*g*)). It is apparent that large von Mises stresses appear at the edge of the contact. Then, the displacement is forced back to the left (i.e., in the negative *X* direction) and shakedown occurs (Fig. 4(*h*)). In other words, the von Mises stress decreases suddenly because of the change in the direction of the tangential force. As it displaces further to the left, the von Mises stress keeps decreasing, and the region of large von Mises stresses starts to show up again at the two edges of the contact area (Figs. 4(*i*)–4(*j*)). The area with large von Mises stresses keeps growing and being stretched (Figs. 4(*k*)–4(*l*)) until it reaches $-1*\omega_c$, where it has a mirror image shape similar to that of the case at $1*\omega_c$ (Fig. 4(*g*)). Another shakedown takes place as the displacement is forced to the right (Fig. 4(*m*)). Finally, the cylinder moves back to $0*\omega_c$ and that completes one cycle of loading (Fig. 4(*n*)). The large von Mises stress appears at the two edges of the contact again. The simulation continues for another five cycles. As shown in Fig. 4(*o*), the large von Mises stress stays there after six cycles of load. The development of the von Mises stresses is also investigated for other interference cases of $0.7*\omega_c$, $2*\omega_c$, and $3*\omega_c$, but the trends remain the same as for the case of $1*\omega_c$ (of course, having larger plastic regions as the interference increases). For brevity, these results are not reported. From the evolution of von Mises stress above, a conclusion can be drawn that during the oscillatory tangential loading, the two contact edges tend to experience the largest von Mises stress. It is, therefore, postulated that cracks and fatigue are most likely to initiate and propagate at the contact edges.

4.2 The Distribution of Plastic Strain. When the von Mises stresses reach the yield strength and fretting is in the elastic-plastic regime, there are plastic strains in the contacting bodies which are indicated by the equivalent plastic strain, ε_p. Figure 5 shows the distribution of ε_p at the region of contact after three cycles of horizontal loading have completed, at different interferences and COFs. In all the three cases, the maximum ε_p is located at the two edges of contact, which coincides with the location of the maximum von Mises stress. That is consistent with the direct correspondence between stress and strain. It can be further explained by the pileup (discussed further in Sec. 4.5) on the surface of the block.

Figure 5(*a*) illustrates the plastic strain distribution at $0.7*\omega_c$ interference with $\mu = 1$. Although there is no plastic strain under surface just after the normal loading (i.e., purely in the elastic regime), the introduction of the tangential force spawns plastic strains that are confined near the contacting surfaces. This also gives rise to friction-induced work. When the interference increases to $1*\omega_c$ (the limit of the elastic regime), as shown in Fig. 5(*b*), the plastic strains increase because of the increase of the normal force caused by the larger interference. As the interference increases further to $3 * \omega_c$ (Fig. 5(*c*)), the plastic strain distributions change. Since the region under the surface reaches plasticity in a much larger area (details provided by Jackson and Green [15]), the plastic strain spreads to a deeper and wider region under

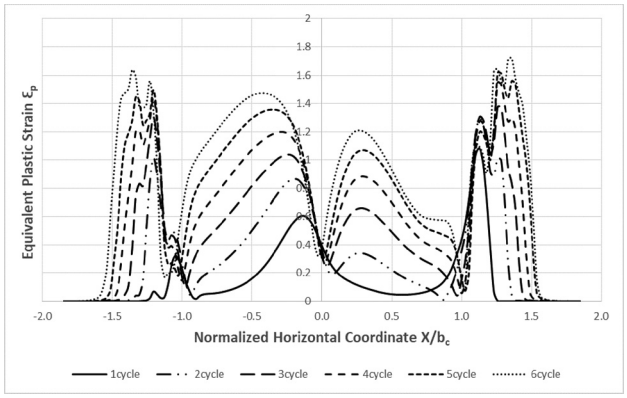

Fig. 6 The distribution of the equivalent plastic strain on the contacting surface of the cylinder at 1*ω_c interference with $\mu = 1$

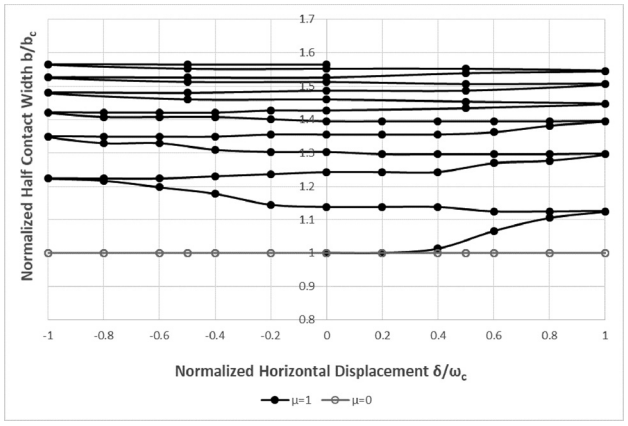

Fig. 7 The development of junction growth at 1*ω_c interference for fictional and frictionless contacts during six cycles of load

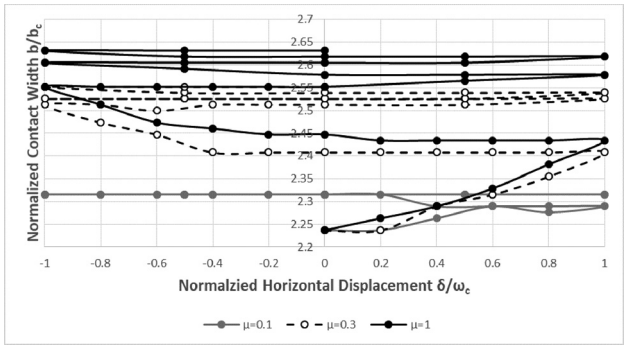

Fig. 8 The development of junction growth at 3*ω_c interference with different COFs during three cycles of load

the surface. Consequently, the larger region absorbs the damage manifested by a deeper scar. As a result, the maximum ε_p (located at the edges) is relatively smaller at larger interference. In other words, as the contact produces more permanent damage, there is less plastic strain at the edges, i.e., at the location where the failure, as postulated in Sec. 4.1, is most likely to show up. Evident from the maximum values in Figs. 5(*c*) ($\mu = 1$) and 5(*d*) ($\mu = 0.3$), the plastic strain decreases with the drop of the COF, especially at the edges.

In order to understand the progression of plastic strain, the distribution of ε_p on the contacting surfaces after each horizontal loading cycle is investigated. Figure 6 represents the evolution of ε_p on the surface of the half cylinder during the six cycles of horizontal load at 1*ω_c interference with $\mu = 1$. The abscissa is the horizontal position on the surface normalized by the critical half contact width b_c (as defined and reported earlier). As shown in Fig. 6, the plastic strain keeps increasing after each cycle of loading. Additionally, the maximum ε_p stays at the right edge of the contact (due to junction growth as discussed in Sec. 4.3, where the edges of contact keep moving laterally outward after each cycle). This phenomenon could be attributed to the decrease of the normal force required to keep the interference. As the oscillatory sliding motion proceeds, the tip of the cylinder keeps being flattened and the normal force required to maintain the same interference continues to decrease. Since, at the very beginning of the horizontal load, the cylinder moves to the right first, the right edge of the contact experiences deformation caused by the pile-up (or the abrupt change of the curvature) on the surface of the block under a larger normal force. As the cylinder returns to the left, under a smaller normal force, the deformation on the left edge of the contact is less than that on the right. Consequently, ε_p is relatively larger on the right edges which are located in the same direction as the initial horizontal motion of the cylinder. The observed directional effect is consistent with the initial direction of motion in the current simulation.

4.3 The Junction Growth. The junction growth, i.e., the increase of the contact area, is observed during the oscillatory horizontal motion for displacement-controlled analysis performed in this work. Figure 7 shows the development of the half contact width, normalized by the critical half contact width, during the six cycles of horizontal displacement at 1∗ω_c interference for frictional ($\mu = 1$) and frictionless contacts. When $\mu = 1$, the frictional contact area keeps increasing, where it tends to stabilize after sufficient cycles of load. But for frictionless contact, the area remains constant. The explanation is that the introduction of the friction force produces plasticity on the contacting surface and consequently increases the contacting width. However, without friction, there is no plastic region on the surface at 1∗ω_c interference, and no plastic strain is caused so that there is no junction growth. To study the effect of COF on the junction growth, different COFs are applied to the model at the same interference. Figure 8 shows the development of half contact width at 3∗ω_c interference during three cycles of load. Two conclusions are drawn from the above observation. First, the magnitude of the junction growth increases with the COF. The explanation is that the small COF introduces small tangential force, which causes less plastic deformation on the surface so that less junction growth is generated. Second, the rate of stabilization decreases as the COF increases, because the normal force keeps decreasing during sliding and the von Mises stress on the surface decreases faster with smaller COF. Consequently, in the cases with smaller COFs, the von Mises stress on the surface falls below the yield strength earlier so that the junction growth stabilizes earlier.

The junction growth is also found even at 0.7∗ω_c interference, but that is combined with fretting (sliding motion) under a COF of $\mu = 1$. Since there is plastic strain at the interface, it is reasonable to expect junction growth. And indeed, there is a 9.7% increase in the contact width after one cycle of horizontal loading.

4.4 The Evolution of the Tangential Force per Unit Length. As the fretting motion proceeds, the output of the tangential force per unit length, Q/L, is recorded. Even with $\mu = 0$, it is found that $Q/L \neq 0$. For instance, the absolute Q/L at 1∗ω_c interference, with $\mu = 0$, ranges from 0 to 573 N/m during the first cycle of the horizontal loading. It is noted, however, that the maximum value of $Q/L = 573$ N/m, by comparison to $Pc/L = 3.873 \times 10^7$ N/m, (i.e., $Q/Pc = 1.5 \times 10^{-5}$), is minute. It is caused by numerical round-off errors, and effectively, it verifies a frictionless case. In contrast, at 1∗ω_c interference and with $\mu = 1$, the absolute Q/L ranges from 0 to 1.79×10^7 N/m during the first

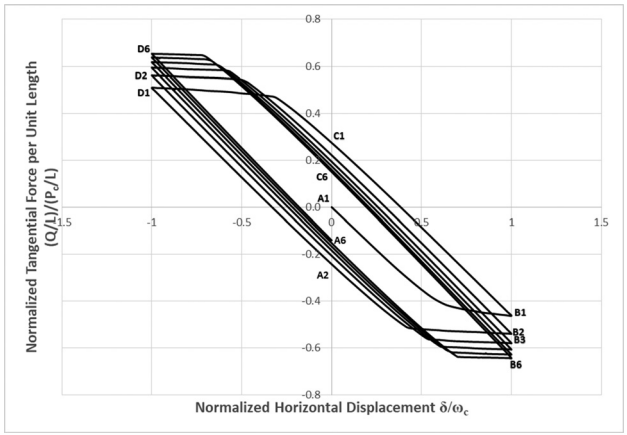

Fig. 9 The development of tangential force at $1^{*}\omega_c$ interference with $\mu = 1$ during six cycles of load

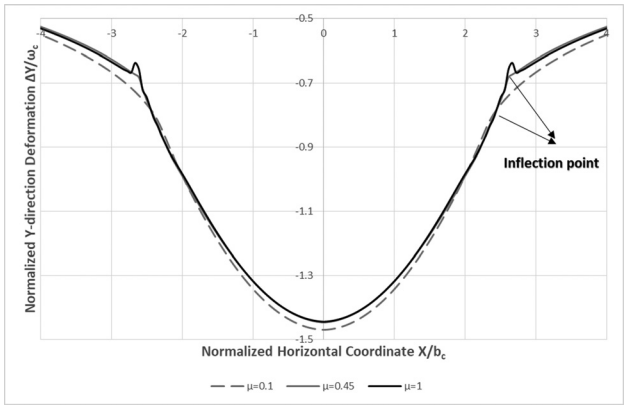

Fig. 11 The scars on the surface of the block at $3^{*}\omega_c$ interference after three cycles of load

cycle of the horizontal loading. Figure 9 shows the development of the Q/L, normalized by critical normal load per unit length P_c/L, during six cycles of loading at $1*\omega_c$ interference with $\mu = 1$. The evolution of the traction force in Fig. 9 begins to stabilize after the first one-quarter of the cycle. The stabilized curve is the typical fretting loop at the initial few cycles of loading (also reported by Walvekar et al. [33]). The enclosed area represents the energy loss caused during the fretting motion. It is evident that the maximum tangential force increases as fretting proceeds. It is caused by the cumulative plastic deformation on the contacting surfaces.

4.5 Scars on the Block. As the fretting motion proceeds, a scar is generated at the surface of the flat block. The scar can be visualized by the deformed curve of that surface. Figure 10 shows the deformed curve at $1*\omega_c$ interference with $\mu = 1$ just after the interference is applied. The curve is identical in shape to that of an elastic half-space with line loading, as given by Johnson [2]. When the curve near the contact is zoomed in (see the inset in Fig. 10), the indentation caused by the interference becomes clearly visible.

The scar grows during the oscillatory horizontal loading. Figure 11 depicts the deformed curves of the surface of the contact region at $3*\omega_c$ interference with $\mu = 0.1$ (gross sliding), $\mu = 0.45$ (partial slip and partial stick), and $\mu = 1$ (fully stick) after three cycles of loading. For $\mu = 0.1$, the depression is the shallowest. For $\mu = 0.45$, the depression is deeper and wider, but the center part of the surface is dragged somewhat upward by the lateral motion. The change of the curvature at the inflection point (the position of the edge of the contact) is more pronounced. For $\mu = 1$, the trends mentioned earlier are intensified, and pileup shows up near the inflection point of the curve. According to the results above, the pileup will occur at the edges of the indentation with a sufficiently large COF, especially in the case of the fully stick. The abrupt change of the curvature or pile-up will further produce the large von Mises stress and plastic deformation at the corresponding position of the contact.

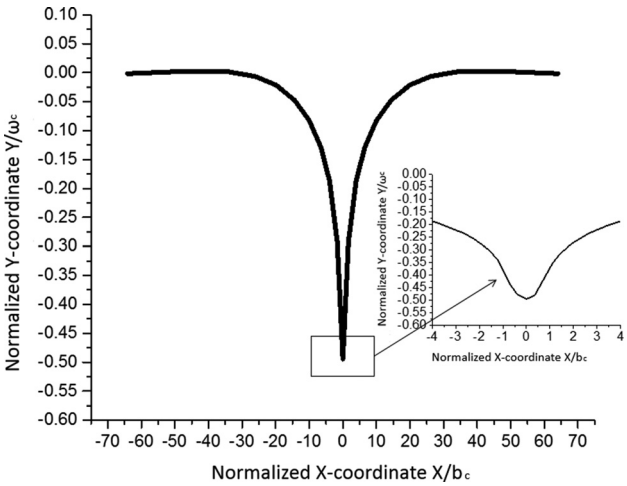

Fig. 10 The curve of the surface of the block after $1^{*}\omega_c$ interference

4.6 The Effect of the Boundary Conditions on the Block. As shown in Table 2, several different types of boundary conditions applied on the four sides of the block are now investigated. The four sides of the block, a_1, a_2, s_1, and s_2, are consistent with Fig. 1. In all six types, the midpoint M on the bottom side a_1 is fixed in the X and the Y direction to ensure the relative motion between the half cylinder and the block. The top of the block is always free. The symbol "+" means the side is fixed in the corresponding direction. Type0 represents the boundary condition where all the results above are generated. The bottom side a_1 is fixed in the X and the Y direction. In Type1, the boundary condition of the bottom side a_1 is changed relative to Type0 to be free in the X direction. In Type2, the boundary conditions of the two sides s_1 and s_2 are changed to be fixed in the X direction relative to Type1. In Type3, the boundary conditions of the two sides s_1 and s_2 are changed to displace $1*\omega_c$ to the right and left, respectively, again relative to Type1. The magnitude of that displacement is changed to be $2*\omega_c$ and $3*\omega_c$ in Type4 and Tpye5, respectively. The displacements on the two sides, s_1 and s_2, generate prestresses in the compressed block. Considering the effect of Poisson's ratio, the top side of the block a_2 will displace Δy

Table 2 Different types of boundary conditions on the four edges of the block (shown in Fig. 1(*a*))

	a_1		s_1		s_2	
Type	X	Y	X	Y	X	Y
0	+	+				
1		+				
2		+	+		+	
3		+	$+1\omega_c$		$-1\omega_c$	
4		+	$+2\omega_c$		$-2\omega_c$	
5		+	$+3\omega_c$		$-3\omega_c$	

Note: "+" represents that the edge is fixed in the corresponding direction. Blank represents the edge is free in the corresponding direction. Edge a_2 is always free, while the midpoint M on the edge a_1 is always fixed in both the X and the Y direction.

upward according to the following. In plane strain, the constitutive equation is

$$\begin{Bmatrix} \sigma_x \\ \sigma_y \\ \sigma_z \\ \tau_{xy} \end{Bmatrix} = \frac{E}{(1+\nu)(1-2\upsilon)} \begin{bmatrix} 1-\nu & \nu & 0 \\ \nu & 1-\nu & 0 \\ \nu & \nu & 0 \\ 0 & 0 & \dfrac{1-2\nu}{2} \end{bmatrix} \begin{Bmatrix} \varepsilon_x \\ \varepsilon_y \\ \gamma_{xy} \end{Bmatrix} \tag{8}$$

According to Eq. (8), the normal stress in the Y direction can be expressed as

$$\sigma_y = \frac{E}{(1+\nu)(1-2\upsilon)} \left[\nu\varepsilon_x + (1-\nu)\varepsilon_y\right] \tag{9}$$

However, $\sigma_y = 0$, before the cylinder is compressed downward, since the top side is set free. Using the condition that the compressive displacement, Δx, is applied on both sides of the block, s_1 and s_2, but in opposite directions, the normal strain in the X direction is compressive

$$\varepsilon_x = -\frac{\Delta x}{2R} \tag{10}$$

According to Eqs. (9) and (10), the normal strain in the Y direction is

$$\varepsilon_y = \frac{\nu}{1-\nu}\frac{\Delta x}{2R} \tag{11}$$

Using the definition of the normal strain in the Y direction

$$\varepsilon_y = \frac{\Delta y}{R} \tag{12}$$

The displacement of the top side, a_2, is therefore

$$\Delta y = \frac{\nu}{1-\nu}\frac{\Delta x}{2} \tag{13}$$

In order to compare the results of the prestressed cases with those of the original cases, Δy must be taken into consideration. If ω is always the interference imposed, as it is the case with no prestress, then the interference in the prestressed case is

$$\omega' = \omega - \Delta y \tag{14}$$

Figure 12 shows the junction growth results of the first quarter of the loading cycle at $1^*\omega_c$ interference with $\mu = 1$ for different

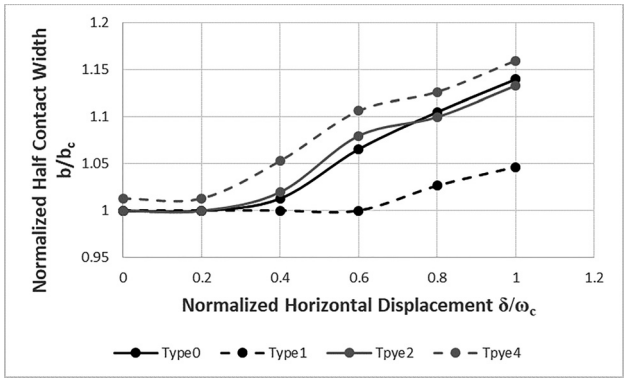

Fig. 12 The junction growth results of the first quarter of the loading cycle at $1^*\omega_c$ interference with $\mu = 1$ in different types of boundary conditions

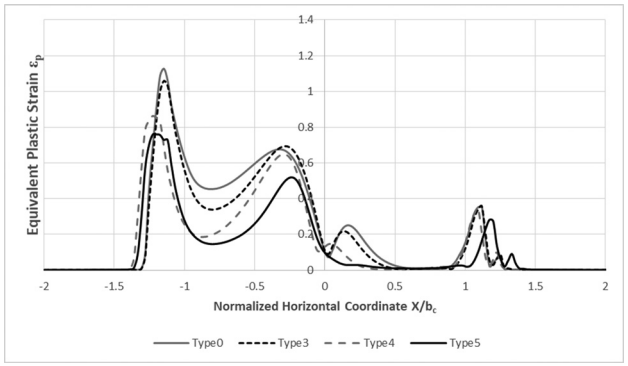

Fig. 13 The distribution of equivalent plastic strain on the surface of the block after one cycle of loading at $1^*\omega_c$ interference with $\mu = 1$ in different types of boundary conditions

types of boundary conditions. It is obvious that the boundary conditions vary the development of the junction growth. Notably, in Type1, the two sides are free to displace laterally outward in the X direction. After the interference is applied, it is equivalent to stretching the block instead of compressing. Therefore, there is a trend of increased junction growth among Type1, Type2, and Type4. In other words, the junction growth increases with the compressive displacement on the two sides (from negative to zero to positive). Additionally, Type0 has the close junction growth with Type2, because the bottom of the block being fixed in the X direction in Type0 introduces a similar effect of the two sides being fixed in the Y direction in Type2. These two conditions characterize most closely the block as a half-elastic space.

Figure 13 illustrates the equivalent plastic strain on the upper surface of the block after one cycle of loading at $1^*\omega_c$ interference with $\mu = 1$ under different types of boundary conditions. It is shown that the plastic strain is larger in Type0 than in any type with a prestress, and it is the smallest in Type5 with two sides displacing $3^*\omega_c$ laterally inward. Therefore, the prestress can reduce the plastic strain on the surface, where the plastic strain decreases with a larger prestress. There are two reasons for that behavior. First, there is σ_z, which elevates the hydrostatic situation (see Eq. (8)), thus reducing the von Mises stress. Second, the negative σ_x opposes the natural tendency of creating a positive σ_x in the fretting sliding motion, which also reduces the von Mises stress during sliding. With smaller von Mises stresses, the corresponding plastic strain is smaller. The compressive prestress is envisioned to also suppress any crack initiation and/or growth at the two edges of the fretting contact.

5 Conclusion

This work presents a 2D plane strain finite element fretting model of a half cylinder in contact with a block. The materials of the two bodies are set to the same elastic-perfectly plastic steel. The fretting model is displacement-controlled, where it is loaded with an interference first, and then a reciprocating horizontal displacement is applied to the top of the half cylinder. Different COFs are used in the model.

Five aspects of the fretting model are studied in this work: the progression of the von Mises stress distribution, the evolution of the plastic strain, the junction growth, the development of tangential force, and the scars on the surface of the block. During the oscillatory tangential loading, the two contact edges tend to experience the largest von Mises stress. It is, therefore, postulated that cracks and fatigue are most likely to initiate and propagate at the contact edges. Likewise, the largest plastic strain shows up at the edges, too. These two phenomena are caused by the abrupt change of the curvature at the edges of the indentation on the surface. When the COF is large enough to reach the fully stick condition, pileup will appear at the position of the abrupt change, which will

intensify the phenomena. The plastic deformation on the surface of the cylinder is not perfectly symmetric about the origin point, where it is slightly larger on the right, which is the direction of the initial motion. This is attributed to the decreasing normal force necessary to maintain a prescribed interference. Also on the right edge, material pileup is larger under a larger normal reaction force relative to the left edge. Due to the plastic deformation of the surfaces, junction growth is found. The magnitude of the junction growth increases with the COFs, while the rate of the convergence of the growth decreases with the COFs. The behavior of the junction growth is found to agree qualitatively with the experimental results [7,9]. Also, larger COF introduces larger tangential forces, which results in larger von Mises stresses. The fretting loop (i.e., the development of the tangential force versus fretting motion) for the initial few cycles of loading is likewise found, where the enclosed area indicates the energy loss. That loop is similar to that found experimentally by Courtney-Pratt and Eisner [7]. Different types of boundary conditions including prestress conditions on the block are applied to the model. It is shown that the boundary conditions vary the junction growth results. Putting forward a design advantage, the prestressed conditions are shown to reduce the residual plastic strain by decreasing the von Mises stresses.

Funding Data

- Department of Energy, Labor and Economic Growth (Project No. 2506U87 and Award No. RH452).

Nomenclature

b = half contact width
b_c = critical half contact width
C = Poisson's ratio parameter
E = elastic modulus
E' = equivalent elastic modulus
p_0 = maximum contact pressure
p_{0c} = critical maximum contact pressure
P/L = normal force per unit length
P_c/L = critical normal force per unit length
Q = tangential force
R = radius of half cylinder
S_y = yield strength
Δx = compressive displacement of the two sides of the block in the case of prestress
Δy = displacement of the top side of the block in the case of prestress
δ = horizontal displacement
ε_p = equivalent plastic strain
ε_x = normal strain in the X direction
ε_y = normal strain in the Y direction
μ = coefficient of friction
ν = Poisson's ratio
σ_e = equivalent von Mises stress
σ_x = normal stress in the X direction
σ_y = normal stress in the Y direction
ω = interference
ω_c = critical interference
ω^* = normalized interference, ω/ω_c
ω' = interference in the case of prestress
ω_1 = the compression of the half cylinder
ω_2 = the compression of the block

Appendix

The interference of a half cylinder in contact with a block is derived below where the dependence of the results on the size of the block is investigated. According to Johnson [2] (taken from p. 130, and shown in Fig. 14(*a*)), the elastic compression of a cylinder in contact with two elastic bodies is obtained. The compression of the upper part of the cylinder O_1C is

$$\delta_1 = \frac{P}{L}\frac{(1-\nu^2)}{\pi E}\left\{2\ln(4R/b_1) - 1\right\} \tag{A1}$$

where the half contact width b_1 is calculated according to the Hertzian theory

$$b_1^2 = 4PR/(\pi L E_1^*) \tag{A2}$$

Here, E_1^* is the composite modulus of the upper body and the cylinder

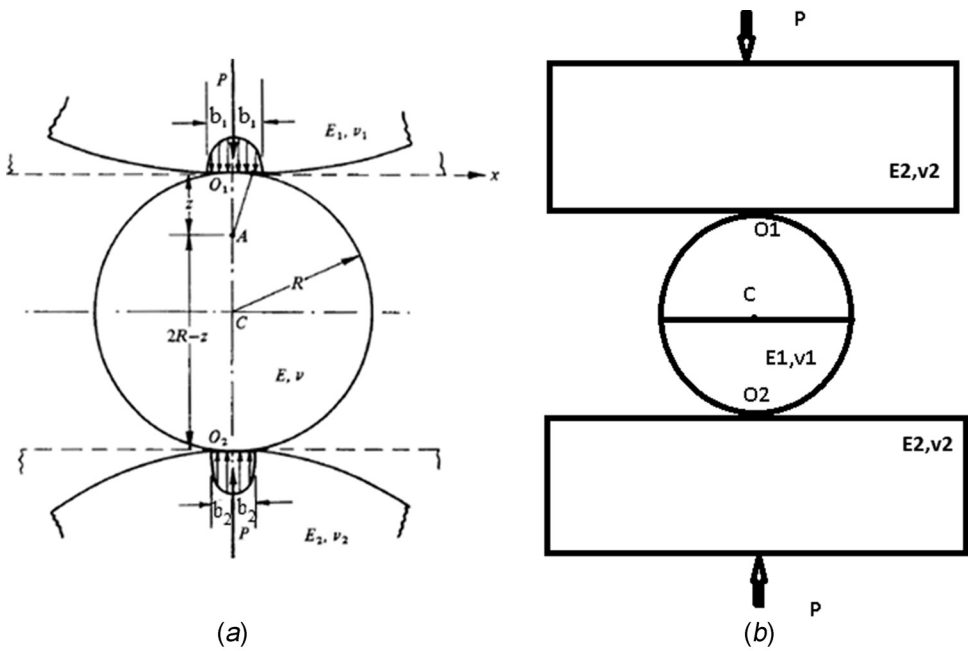

Fig. 14 The contact model to derive the compression of the elastic cylinder in contact with an elastic block: (*a*) the model in contact mechanics by Johnson [2] and (*b*) the equivalent model of the compression of the half cylinder herein

Table 3 Comparison of the critical values between theoretical predictions and FEA results for a half-cylinder of radius is *R*, in contact with a 4*d* × *d* block, of depth, *d*

	Theoretical predictions					FEA results							
d/R	Eq. (7) ω_c (mm)	Eq. (5) b_c (mm)	Eq. (6) P_c/L (MN/m)	C*S$_y$ p_{0c} (GPa)	S_y σ_{emax} (GPa)	b_c (mm)	% dif	P_c/L (MN/m)	% dif	p_{0c} (GPa)	% dif	σ_{emax} (GPa)	% dif
0.25	0.7732	14.88	38.73	1.657	0.9115	14.60	−1.86	37.14	−4.11	1.625	−1.94	0.9842	7.99
0.5	0.8499	14.88	38.73	1.657	0.9115	14.84	−0.28	37.80	−2.41	1.636	−1.28	0.9361	2.71
1	0.9266	14.88	38.73	1.657	0.9115	15.20	2.17	38.56	−0.43	1.645	−0.75	0.9122	0.08
2	1.0033	14.88	38.73	1.657	0.9115	14.80	−0.52	37.52	−3.12	1.625	−1.94	0.9108	−0.07
4	1.0800	14.88	38.73	1.657	0.9115	15.20	2.17	37.88	−2.20	1.623	−2.08	0.9089	−0.28

Note: The ratio d/R is varied from $0.25R$ to $4R$. The equation $C^*S_y = p_{0c}$ is according to Green [32]. Herein, $R = 0.5$ m, $\nu_1 = \nu_2 = 0.32$, $E_1 = E_2 = 200$ GPa, and $S_y = 0.9115$ GPa.

$$\frac{1}{E_1^*} = \frac{1-\nu_1^2}{E_1} + \frac{1-\nu^2}{E} \tag{A3}$$

The model of interest in this work is that of a half cylinder in contact with a block. For that, we use the equivalent model shown in Fig. 14(*b*). The horizontal axis of the half cylinder (passing through point *C*) is prescribed to have a vertical displacement, ω, which is defined as the interference. That interference consists of two parts, the compression of the half cylinder, ω_1, and the compression under the centerline of the block, ω_2. For ω_1, Eq. (A1) yields the compression of the lower half cylinder

$$\omega_1 = \frac{P}{L}\frac{(1-\nu_1^2)}{\pi E_1}\{2\ln(4R/b) - 1\} \tag{A4}$$

where b is the half contact width between the cylinder and the block. The parameters E_1, ν_1, and R belong to the half cylinder. For ω_2, according to Johnson [2], the compression under the centerline of the block is equal to the compression of a half-space under the load of the Hertzian pressure relative to a point at a depth, d. Hence

$$\omega_2 = \frac{P}{L}\frac{(1-\nu_2^2)}{\pi E_2}\{2\ln(2d/b) - \nu_2/(1-\nu_2)\} \tag{A5}$$

The interference is then the addition of Eqs. (A4) and (A5)

$$\omega = \frac{P}{L}\frac{(1-\nu_1^2)}{\pi E_1}\{2\ln(4R/b) - 1\} + \frac{P}{L}\frac{(1-\nu_2^2)}{\pi E_2}\{2\ln(2d/b) - \nu_2/(1-\nu_2)\} \tag{A6}$$

Herein, $\nu_1 = \nu_2 = \nu$, $E_1 = E_2 = E$, and $d = R$. By substituting Eqs. (2) and (3) into Eq. (A6), the interference simplifies to

$$\omega = \frac{P/L}{2\pi E'}\left\{2\ln\left(\frac{2\pi RE'}{P/L}\right) - \frac{1}{1-\nu}\right\} \tag{A7}$$

To verify the assumption of viewing the block as a half-elastic space, different dimensions of the block have been used to compare FEA results with theoretical predictions, where % dif, as given in Table 3, indicates the relative percentage difference between them. According to the table, the FEA results agree very well with the results calculated according to Eqs. (5)–(7), when the depth varies from 0.5R to 4R. When the depth is 0.25R, however, the maximum von Mises stress predicted by the FEA has a somewhat larger deviation from the theoretical value (7.99%). While that indicates that the boundary conditions applied on the block start to affect the stress distribution in the area of the contact, the other differences are still quite low. So, a block of depth, d, that equals to R can clearly be regarded as a half-elastic space. Indeed in this work, all reported results are specifically given for that case of $d = R$. Moreover, the nondimensionalized results in this work can safely be applied to blocks with depths that are about 0.5R or larger. That proposition conforms to the classical Saint-Venant's Principle, which reassures that the critical interferences between two cylinders, as derived by Green [32] in Eq. (24), and the one derived herein for the contact of a half-cylinder against a block in Eq. (7), match closely with a mere 5% difference.

References

[1] Slack, T. S., Leonard, B. D., and Sadeghi, F., 2013, "Estimating Life Scatter in Fretting Fatigue Crack Initiation," Tribol. Trans., **56**(4), pp. 531–535.
[2] Johnson, K. L., 1987, *Contact Mechanics*, Cambridge University Press, New York.
[3] Cattaneo, C., 1938, "Sul Contatto Di Due Corpi Elastici: Distribuzione Locale Degli Sforzi," Rend. Accad. Naz. Lincei, **27**(6), pp. 342–348.
[4] Mindlin, R., 1949, "Compliance of Elastic Bodies in Contact," ASME J. Appl. Mech., **16**, pp. 259–268.
[5] Goodman, L., and Hamilton, G., 1966, "The Stress Field Created by a Circular Sliding Contact," ASME J. Appl. Mech., **33**(2), pp. 371–376.
[6] Adams, G. G., 2014, "Stick, Partial Slip and Sliding in the Plane Strain Micro Contact of Two Elastic Bodies," R. Soc. Open Sci., **1**(3), p. 140363.
[7] Courtney-Pratt, J., and Eisner, E., 1957, "The Effect of a Tangential Force on the Contact of Metallic Bodies," Proc. R. Soc. London, Ser. A, **238**(1215), pp. 529–550.
[8] Tabor, D., 1959, "Junction Growth in Metallic Friction: The Role of Combined Stresses and Surface Contamination," Proc. R. Soc. London, Ser. A, **251**(1266), pp. 378–393.
[9] Parker, R., and Hatch, D., 1950, "The Static Coefficient of Friction and the Area of Contact," Proc. Phys. Soc. London Sect. B, **63**(3), p. 185.
[10] Leonard, B. D., Sadeghi, F., Evans, R. D., Doll, G. L., and Shiller, P. J., 2009, "Fretting of WC/aC: H and Cr2N Coatings Under Grease-Lubricated and Unlubricated Conditions," Tribol. Trans., **53**(1), pp. 145–153.
[11] Leonard, B. D., Sadeghi, F., Shinde, S., and Mittelbach, M., 2012, "A Novel Modular Fretting Wear Test Rig," Wear, **274–275**, pp. 313–325.
[12] Warhadpande, A., Leonard, B., and Sadeghi, F., 2008, "Effects of Fretting Wear on Rolling Contact Fatigue Life of M50 Bearing Steel," Proc. Inst. Mech. Eng., Part J, **222**(2), pp. 69–80.
[13] Leonard, B., Sadeghi, F., and Cipra, R., 2008, "Gaseous Cavitation and Wear in Lubricated Fretting Contacts," Tribol. Trans., **51**(3), pp. 351–360.
[14] Kogut, L., and Etsion, I., 2002, "Elastic–Plastic Contact Analysis of a Sphere and a Rigid Flat," ASME J. Appl. Mech., **69**(5), pp. 657–662.
[15] Jackson, R. L., and Green, I., 2005, "A Finite Element Study of Elasto-Plastic Hemispherical Contact against a Rigid Flat," ASME J. Tribol., **127**(2), pp. 343–354.
[16] Tsukizoe, T., and Hisakado, T., 1968, "On the Mechanism of Contact Between Metal Surfaces—Part 2: The Real Area and the Number of the Contact Points," ASME J. Lubr. Technol., **90**(1), pp. 81–88.
[17] Sharma, A., and Jackson, R. L., 2017, "A Finite Element Study of an Elasto-Plastic Disk or Cylindrical Contact against a Rigid Flat in Plane Stress With Bilinear Hardening," Tribol. Lett., **65**(3), p. 112.
[18] Brizmer, V., Kligerman, Y., and Etsion, I., 2007, "A Model for Junction Growth of a Spherical Contact Under Full Stick Condition," ASME J. Tribol., **129**(4), pp. 783–790.
[19] Chang, L., and Zhang, H., 2007, "A Mathematical Model for Frictional Elastic-Plastic Sphere-on-Flat Contacts at Sliding Incipient," ASME J. Appl. Mech., **74**(1), pp. 100–106.
[20] Vijaywargiya, R., and Green, I., 2007, "A Finite Element Study of the Deformations, Forces, Stress Formations, and Energy Losses in Sliding Cylindrical Contacts," Int. J. Non-Linear Mech., **42**(7), pp. 914–927.
[21] Boucly, V., Nélias, D., and Green, I., 2007, "Modeling of the Rolling and Sliding Contact Between Two Asperities," ASME J. Tribol., **129**(2), pp. 235–245.

[22] Gupta, V., Bastias, P., Hahn, G. T., and Rubin, C. A., 1993, "Elasto-Plastic Finite-Element Analysis of 2-D Rolling-Plus-Sliding Contact With Temperature-Dependent Bearing Steel Material Properties," Wear, **169**(2), pp. 251–256.
[23] Ghosh, A., Leonard, B., and Sadeghi, F., 2013, "A Stress Based Damage Mechanics Model to Simulate Fretting Wear of Hertzian Line Contact in Partial Slip," Wear, **307**(1), pp. 87–99.
[24] Mohrbacher, H., Celis, J.-P., and Roos, J., 1995, "Laboratory Testing of Displacement and Load Induced Fretting," Tribol. Int., **28**(5), pp. 269–278.
[25] Brandt, J., Charron, K., Zhao, L., MacDonald, S., and Medley, J., 2011, "Commissioning of a Displacement-Controlled Knee Wear Simulator and Exploration of Some Issues Related to the Lubricant," Proc. Inst. Mech. Eng., Part H, **225**(8), pp. 736–752.
[26] Johnson, T., Laurent, M., Yao, J., and Gilbertson, L., 2001, "The Effect of Displacement Control Input Parameters on Tibiofemoral Prosthetic Knee Wear," Wear, **250**(1), pp. 222–226.
[27] Lanovaz, J., and Ellis, R., 2008, "Dynamic Simulation of a Displacement-Controlled Total Knee Replacement Wear Tester," Proc. Inst. Mech. Eng., Part H, **222**(5), pp. 669–681.
[28] Shigley, J. E., and Mischke, C. R., 1989, *Mechanical Engineering Design*, 5th ed., McGraw-Hill, New York.
[29] Jiang, Y., Zhang, M., Park, T.-W., and Lee, C.-H., 2004, "An Experimental Study of Self-Loosening of Bolted Joints," ASME J. Mech. Des., **126**(5), pp. 925–931.
[30] Kenny, P., and Johnson, S., 1976, "An Investigation of the Abrasive Wear of Mineral-Cutting Tools," Wear, **36**(3), pp. 337–361.
[31] Barber, J. R., 1992, *Elasticity*, Kluwer Academic Publishers, Dordrecht, The Netherlands.
[32] Green, I., 2005, "Poisson Ratio Effects and Critical Valus in Spherical and Cylindrical Hertzian Contacts," Appl. Mech. Eng., **10**(3), pp. 451–462.
[33] Walvekar, A. A., Leonard, B. D., Sadeghi, F., Jalalahmadi, B., and Bolander, N., 2014, "An Experimental Study and Fatigue Damage Model for Fretting Fatigue," Tribol. Int., **79**, pp. 183–196.